RESEARCH ARTICLE

Simultaneous multislice rapid magnetic resonance elastography of the liver

Waqas Majeed[1] (ORCID) | Prateek Kalra[1] | Arunark Kolipaka[1,2,3]

[1]Department of Radiology, The Ohio State University Wexner Medical Center, Columbus, Ohio, USA

[2]Department of Biomedical Engineering, The Ohio State University, Columbus, Ohio, USA

[3]Department of Internal Medicine - Division of Cardiology, The Ohio State University Wexner Medical Center, Columbus, Ohio, USA

Correspondence
Arunark Kolipaka, PhD, 395 West 12th Avenue, 4th Floor, Department of Radiology, The Ohio State University Wexner Medical Center, Columbus OH 43210, USA
Email: arunark.kolipaka@osumc.edu

To design and validate a rapid Simultaneous Multi-slice (SMS) Magnetic Resonance Elastography technique (MRE), which combines SMS acquisition, in-plane undersampling and an existing rapid Magnetic Resonance Elastography (MREr) scheme to allow accelerated data acquisition in healthy volunteers and comparison against MREr. SMS-MREr sequence was developed by incorporating SMS acquisition scheme into an existing MREr sequence that accelerates MRE acquisition by acquiring data during opposite phases of mechanical vibrations. The MREr sequence accelerated MRE acquisition by acquiring data during opposite phases of mechanical vibrations. Liver MRE was performed on 23 healthy subjects using MREr and SMS-MREr sequences, and mean stiffness values were obtained for manually drawn regions of interest. Linear correlation and agreement between MREr- and SMS-MREr-based stiffness values were investigated. SMS-MREr reduced the scan time by half relative to MREr, and allowed acquisition of four-slice MRE data in a single 17-second breath-hold. Visual comparison suggested agreement between MREr and SMS-MREr elastograms. A Pearson's correlation of 0.93 was observed between stiffness values derived from MREr and SMS-MREr. Bland–Altman analysis demonstrated good agreement, with −0.08 kPa mean bias and narrow limits of agreement (95% CI: 0.23 to −0.39 kPa) between stiffness values obtained using MREr and SMS-MREr. SMS can be combined with other fast MRE approaches to achieve further acceleration. This pushes the limit on the acceleration that can be achieved in MRE acquisition, and makes it possible to conduct liver MRE exams in a single breath-hold.

KEYWORDS
hepatobiliary, magnetic resonance elastography, parallel imaging, SMS, SMS-MRE

1 | INTRODUCTION

Hepatitis B and C, nonalcoholic fatty liver disease and alcohol abuse, etc., cause liver fibrosis, which is one of the leading causes of death worldwide, and is accompanied by increased liver stiffness.[1] It can progress into liver cirrhosis if left untreated, which cannot be

cured. However, liver fibrosis has been shown to be reversible if detected early.[2,3] Therefore, early detection of liver fibrosis has immense clinical value.

Liver biopsy is the current clinical gold standard for diagnosis and staging of liver fibrosis. However, it has some major limitations and, given the spatial heterogeneity of the disease and the sampling error, biopsy may result in misdiagnosis.[4] Additionally, this procedure can result in complications due to its invasive nature.[5] Noninvasive techniques including ultrasound elastography and magnetic resonance elastography (MRE) have overcome the drawbacks of liver biopsy and emerged as promising tools for the diagnosis and staging of liver fibrosis.

MRE is a noninvasive technique for assessment of tissue stiffness. It involves introduction of waves into the tissue using an external driver, imaging of these waves using a phase-contrast MRI sequence, and computation of stiffness maps by applying an inversion algorithm to the imaged waves.[6] Feasibility of MRE for stiffness estimation in liver, brain, heart, breast, aorta and lungs has been demonstrated.[7-13] In particular, liver MRE is increasingly being used for the diagnosis and staging of liver fibrosis[14-16] by allowing noninvasive high resolution mapping of liver stiffness.

Liver MRE requires acquisition under breath-holds to avoid motion artifacts, and therefore can immensely benefit from accelerated image acquisition. Current clinical protocols for liver MRE data acquisition require one ~ 16–18-second breath-hold per slice, with an in-plane acceleration factor of 1.4.[15,17] The inherent variation between breath-holds results in variation in the orientations of the acquired slices. Also, the interslice gap may not be uniform across the slices. Therefore, multiple breath-hold acquisitions may limit the anatomical precision that can be achieved using MRE.

Chamarthi et al proposed a method (referred to as rapid MRE [MREr]) to reduce the acquisition time by acquiring data with the same motion-encoding gradient (MEG) polarities during opposing phases of mechanical vibration.[18] Although MREr reduces the breath-hold duration by 50%, multiple breath-holds are still needed for the acquisition of multislice data (typically four slices) used for clinical diagnosis. Other techniques, such as eXpresso MRE,[19] use a fractional encoding scheme to simultaneously encode multiple slices per wave cycle to accelerate the acquisition. Generally, the fractional encoding scheme has lower phase sensitivity compared with the full MEG used in standard gradient recalled echo (GRE)-MRE. However, it is important to understand that depending on the type of tissue being imaged (ie, with short $T2*$), the phase-to-noise ratio can be higher compared with the full encoding scheme, as echo times can be shortened in fractional encoding.[20] There exist spin-echo (SE)-based approaches for efficient MRE encoding along multiple directions, such as sample interval modulation (SLIM)-MRE.[21] SLIM-MRE applies MEG in all the spatial directions during the same readout and shifts the MEGs in such a way so as to capture 3D waves in different harmonics of the temporal Fourier transform. However, SLIM-MRE has a relatively long TE compared with a standard MRE sequence and has concomitant gradient field effects. While the SLIM-phase varying technique[22] has the same TE as the standard MRE sequence, it suffers from nonuniform flow compensation. The use of SE-echo planar imaging (EPI) has been proposed to perform highly accelerated MRE examinations to cover a large volume of the liver, allowing a single breath-hold (ie, 19–32 seconds) liver MRE for a single encoding direction.[23] However, geometric distortion due to Bo inhomogeneities in the phase-encode direction can result in an inaccurate stiffness estimate.[24] Furthermore, EPI suffers from other artifacts, such as N/2 ghosting and chemical shift from fat, which might be potential problems when imaging the liver. Similarly, spiral MRE that has been initially implemented in the brain[25,26] can potentially be used in the liver. As a spiral MRE sequence is more robust to motion and has relatively higher signal-to-noise ratio (SNR) efficiency compared with Cartesian sampling techniques. However, a spiral sequence has limitations with respect to eddy current artifacts and spiral artifacts, which can further bias the stiffness estimates. A compressed sensing-based liver MRE technique, a Bayesian method for MRE using approximate message passing (BEAM), was implemented[27] with random sampling, which could accelerate the liver MRE scans. However, this technique is computationally intensive[28] and potentially requires a graphic processing unit to reconstruct the images on the scanner.

Simultaneous multislice (SMS) excitation has shown tremendous utility in achieving high acceleration factors for various applications.[29-31] However, its utility in accelerating MRE acquisition has not been fully explored. The use of SMS without in-plane undersampling to accelerate MRE acquisition has been reported previously in the brain.[32] Compared with in-plane acceleration, SMS acceleration results in a gain in SNR, which can be traded for acceleration, eg, by adding in-plane acceleration, reducing the number of phase offsets acquired or reduced motion sensitivity (fractional encoding) and shorter TR/TE.[19,20,33] No studies to date have investigated whether a combination of SMS and in-plane acceleration can be used for MRE acquisition with adequate quality, despite the additional g-factor penalty introduced by incorporation of SMS. Even more challenging is combining SMS and in-plane acceleration with MREr, which already has lower SNR compared with traditional acquisition due to reduced TR.[18]

In this study, we propose the incorporation of SMS acquisition into MREr with in-plane acceleration (SMS-MREr) to enable the acquisition of clinical four-slice liver MRE data within one 17-second breath-hold. We hypothesize that elastograms with SMS-MREr will be consistent with those with MREr. To our knowledge, this is the first study that utilizes SMS along with in-plane acceleration for MRE.

2 | THEORY

2.1 | MREr

MRE sequences are designed to encode vibratory motion introduced by an external driver by playing MEGs. In a commonly used GRE-MRE-based acquisition scheme, images with positive and negative vibration encoding are acquired by playing MEGs with opposing polarities during the same

phase of external vibration in different TRs. TR, therefore, needs to be a multiple of the time period of mechanical vibrations to ensure that image acquisition is synchronized with mechanical vibrations (Figure 1A). For instance, the minimum whole-number TR with a vibration frequency of 60 Hz is 50 ms, ie, three vibration cycles. In MREr, images with positive and negative encodings are acquired by playing MEGs with the same polarity during opposing phases of mechanical vibration (Figure 1B). This makes it possible to make TR equal to integer-and-a-half times the period of mechanical vibrations. Therefore, MREr allows a 50% reduction in TR, resulting in half the scan time. For instance, the minimum whole number TR for MREr is 1.5 cycles for a vibration frequency of 60 Hz. Shorter TRs employed in MREr result in some loss in SNR. However, excellent agreement between MREr and traditional acquisitions has been demonstrated.[18]

2.2 | SMS acquisition and controlled aliasing in parallel imaging results in higher acceleration

An SMS acquisition employs multiband pulses to simultaneously excite and acquire multiple slices.[34] The simultaneously excited slices are collapsed into a single image. The acceleration achieved due to SMS excitation is equal to the number of simultaneously excited slices, hereafter referred to as the multiband factor (MB). SMS excitation can be combined with in-plane acceleration, resulting in in-plane aliasing of the collapsed slices. These collapsed voxels can be separated when the data are acquired using multiple coils, as long as the matrix of coil sensitivities at the collapsed voxels is not ill-conditioned. Insufficient variation in coil sensitivity at collapsed voxels results in noise amplification characterized by the "geometry factor" or "g-factor".[35] Typically, coil sensitivity variation in the slice direction is not sufficient to allow separation of slices when the gap between simultaneously excited slices is small. To address this, controlled aliasing in parallel imaging results in higher acceleration (CAIPIRIHNA)-based acquisition schemes are utilized to effectively shift one or more slices in the phase-encode direction.[35] In spoiled GRE sequences, an RF-based CAIPIRINHA approach is used, where the slices are mutually shifted by introducing a slice-dependent phase variation in the phase-encode direction (k_y) by altering the RF pulse phase. This shift between simultaneously excited slices allows the reconstruction to benefit from variation in coil sensitivity in the phase-encode direction. The effect of in-plane undersampling and CAIPIRINHA can be understood from Figure 2A. In-plane undersampling results in aliasing, whereas CAIPIRINHA results in a shift in the phase-encode direction (middle row). The magnitude image for an acquisition with MB = 2, 2-fold in-plane undersampling and a CAIPIRINHA shift equal to 1/4 of the phase field of view (FOV) is shown in Figure 2B, top row.

2.3 | Split slice-generalized autocalibrating partially parallel acquisitions reconstruction

Split slice-generalized autocalibrating partially parallel acquisitions (GRAPPA) is a k-space-based approach to separate simultaneously acquired slices.[36] It can be used with or without in-plane undersampling. A fully sampled, low-resolution reference scan is required to fit kernels for the
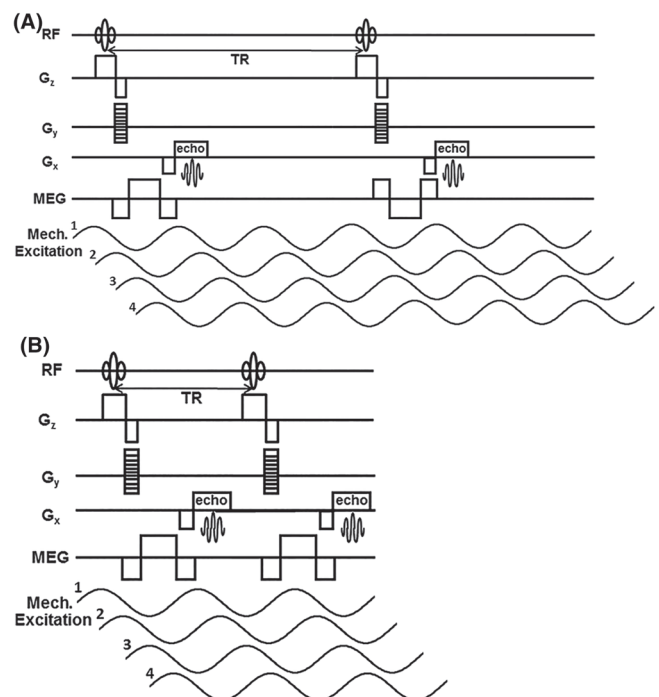
FIGURE 1 Gradient recalled echo-magnetic resonance elastography (GRE-MRE) and rapid magnetic resonance elastography (MREr) sequences. (A) Simplified sequence diagram of a GRE-based MRE sequence. Motion-encoding gradients (MEGs) with alternating polarities are played every TR for positive and negative motion encoding, respectively. The GRE-MRE sequence used clinically for liver MRE typically employs three cycles of external vibration synchronized to the TR (ie, 50 ms). (B) Simplified MREr sequence diagram. MEGs with same polarity are played during opposing phases of mechanical vibration to achieve positive and negative encoding, thus reducing the required TR to 1.5 cycles of external vibration. In both sequences, imaging is repeated for four phase offsets with respect to the mechanical excitation
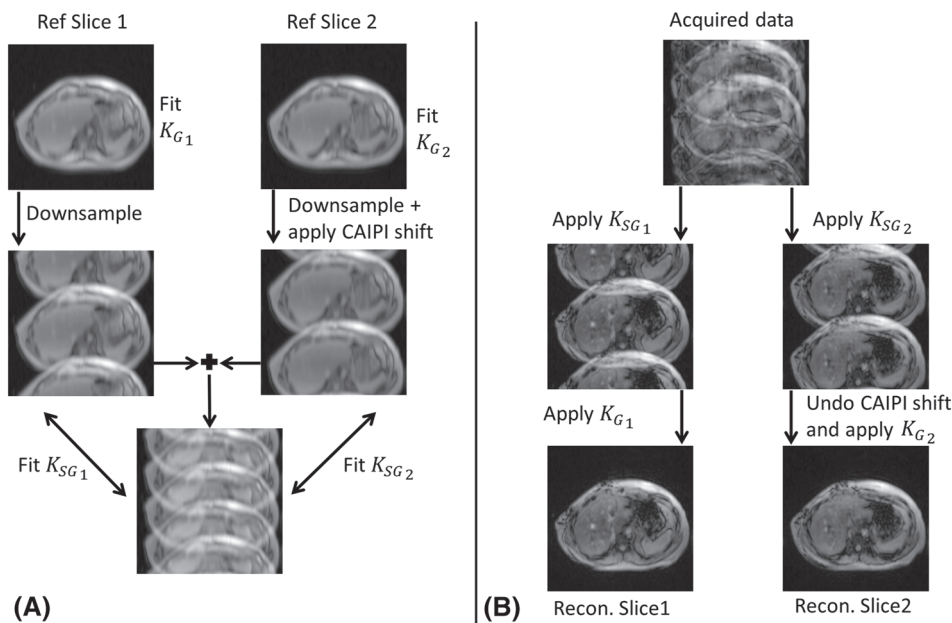
FIGURE 2 (A) Kernel fitting on reference data for R = multiband factor (MB) = 2. All the operations are performed in k-space, but magnitude images are displayed for visualization purposes. Slices 1 and 2 represent slices that are acquired simultaneously in the accelerated magnetic resonance elastography (MRE) acquisition. Row 1: low-resolution fully sampled reference data are used to fit in-plane generalized autocalibrating partially parallel acquisitions (GRAPPA) kernels (K_{G_1} and K_{G_2}) for individual slices. Row 2: k-space data from individual slices are undersampled and phase-shifted to match in-plane acceleration and controlled aliasing in parallel imaging results in higher acceleration (CAIPIRINHA) shift for the accelerated MRE acquisition. Row 3: images in row 2 are added. Split slice-GRAPPA kernel fitting is performed, with row 3 as source and row 2 as target k-spaces, to obtain slice-GRAPPA kernels K_{SG_1} and K_{SG_2}. Please note that K_{SG_1} and K_{G_1} etc. represent sets of kernels fitted to individual coil elements.
(B) Reconstruction of data for R = MB = 2. All the operations are performed in k-space, but magnitude images are displayed for visualization purposes. Row 1: data acquired with in-plane as well as slice acceleration. Row 2: slice-GRAPPA kernels K_{SG_1} and K_{SG_2} are applied to the acquired data to obtain k-space for separated slices, which are still CAIPIRINHA-shifted and undersampled by in-plane acceleration factor. Row 3: in-plane GRAPPA kernels K_{G_1} and K_{G_2} are applied to the k-spaces of the separated slices after undoing the CAIPIRINHA shift to obtain fully reconstructed images

separation of slices as well as filling in the missing lines due to in-plane acceleration. Mathematical details of this approach can be found in Cauley et al.[36] Here, we briefly describe reconstruction steps for data acquired with SMS combined with in-plane undersampling:

1. Kernels are fitted to fill the missing lines due to in-plane acceleration on individual reference slices (Figure 2A, row 1).

   Reference k-space data are undersampled and phase-shifted according to the utilized CAIPIRINHA scheme (Figure 2A, row 2), and then added to simulate SMS acquisition with in-plane undersampling (Figure 2A, row 3). Kernels are fitted using a split slice-GRAPPA approach to fit k-space of the undersampled/CAIPIRINHA shifted images from the acquired data

2. Simultaneously acquired MRE slices (Figure 2B, row 1) are separated in k-space using the kernels fitted in step 2 (Figure 2B, row 2). These slices are still CAIPIRINHA-shifted and undersampled in k-space.

3. In-plane GRAPPA kernels (fitted in step 1) are applied to the separated slices after undoing the CAIPIRINHA shift to obtain fully reconstructed images.

We used the split slice-GRAPPA algorithm for reconstruction because it has been shown to reduce interslice leakage.[36]

2.4 | Spurious phase contributions in MRE

As seen in Figure 1, images with four phase offsets between MEG and vibrations with positive as well as negative encoding are acquired in GRE-MRE as well as in MREr, resulting in eight images per slice. The resultant phase images are referred to as $PO_0^+, PO_0^-, PO_{\pi/2}^+, PO_{\pi/2}^-, PO_\pi^+, PO_\pi^-, PO_{3\pi/2}^+$ and $PO_{3\pi/2}^-$, where PO is the phase offset, the subscript represents MEG phase offset relative to the MEG used for the first encoding, and the superscript represents the polarity of encoding. The phase in each of these images contains contributions from thermal noise (ϕ_{PN}), off-resonance (ϕ_{B_0}), eddy currents (ϕ_{EC}), concomitant fields (ϕ_{CF}) and motion sensitization due to MEGs (ϕ_{MEG}) and imaging gradients (ϕ_{IG}). ϕ_{EC} includes the motion-sensitive contribution due to eddy currents. ϕ_{B_0} and ϕ_{CF} are independent of MEG polarity and phase offset. Let PO_θ^s be one of the phase offset images, where $\theta \in \left\{0, \frac{\pi}{2}, \pi, \frac{3\pi}{2}\right\}$ and $s \in \{+, -\}$, then

$$PO_\theta^s = \phi_{B_0} + \phi_{CF} + \phi_{PN}^{\theta s} + \phi_{EC}^{\theta s} + \phi_{IG}^{\theta s} + \phi_{MEG}^{\theta s} \tag{1}$$

where the superscript on the right-hand side represents variation across phase offsets and encoding polarities. The dependence of these on phase offset and encoding polarity is summarized as

$$\phi_{MEG}^{\theta +} = -\phi_{MEG}^{\theta -} = -\phi_{MEG}^{(\theta + \pi) +} \tag{2}$$

$$\phi_{IG}^{\theta s} = -\phi_{IG}^{(\theta + \pi) s} \tag{3}$$

2.5 | In-plane acceleration, SMS and phase noise

Parallel imaging reduces SNR due to two reasons: first, the acquisition of fewer k-space lines increases noise standard deviation by $\sqrt{R}$, where R is the in-plane acceleration factor[37,38]; second, the separation of the voxels aliased as a result of parallel imaging results in a spatially varying amplification of noise by the g-factor[30,38]. Thus

$$SNR_{Acc}(x,y) = \frac{SNR_{NoAcc}(x,y)}{g(x,y)\sqrt{R}} \tag{4}$$

where $SNR_{Acc}(x,y)$, $SNR_{NoAcc}(x,y)$ and $g(x,y)$ represent SNR with parallel imaging, SNR without parallel imaging and g-factor as a function of spatial location. Because phase standard deviation is inversely proportional to image SNR[39],

$$\frac{\sigma_{\phi_{Acc}}(x,y)}{\sigma_{\phi_{NoAcc}}(x,y)} \propto g(x,y)\sqrt{R} \tag{5}$$

where $\sigma_{\phi_{Acc}}(x,y)$ and $\sigma_{\phi_{NoAcc}}(x,y)$ represent phase standard deviation with and without parallel imaging, respectively, as a function of position.

Thus parallel imaging results in an increase in phase noise. In-plane acceleration techniques such as GRAPPA result in penalties due to $\sqrt{R}$ as well as $g(x,y)$. However, SMS acceleration without k-space undersampling results in a g-factor penalty only. With the appropriate use of CAIPIRINHA, the aliasing pattern in the phase-encode direction remains unchanged when SMS acceleration is used instead of in-plane acceleration. Consequently, for spatially close simultaneously excited slices, g-factor for a given MB is very similar to that with an identical R. In contrast to in-plane acceleration, multislice acceleration does not suffer from $\sqrt{R}$ penalty, and therefore can be the preferred choice for accelerated imaging for multislice acquisitions.

3 | MATERIALS AND METHODS

The protocol was approved by the institutional review board. Written informed consent was obtained and documented for all volunteers. Twenty-three healthy subjects (16 males and seven females) aged 22–74 years participated in this study.

3.1 | Image acquisition

All imaging was performed on a 1.5 T MRI scanner (Aera, Siemens, Erlangen, Germany).

3.1.1 | Human volunteers

Standard vendor-provided body matrix and spine coils were used as receive coils (Siemens); 10–20 receive channels were automatically selected by the scanner software based on coil placement and slice prescription. A commercial pneumatic driver system was used to introduce 60 Hz mechanical vibrations in each subjects liver (Resoundant, Mayo Clinic Foundation, Rochester, MN). The passive driver was placed anterior on the subject's body close to the liver and secured with an elastic belt. The passive driver was connected via a plastic tube to the active driver, which was placed outside the scan room to induce 60 Hz vibrations into the liver.

MREr[18] and the developed SMS-MREr sequences were used to acquire MRE data. Figure 1B shows the sequence diagram of MREr, where the polarity of the MEGs remains the same in each TR, but the TR is adjusted to fit 1.5 cycles of the external motion instead of three cycles. Multiband pulses with the CAIPIRINHA phase-cycling scheme were incorporated into the MREr sequence to develop the SMS-MREr sequence.

The following imaging parameters were identical for both the MREr and SMS-MREr sequences: TE = 21.4 ms; TR = 25 ms; FOV = 360 x 360 mm^2; flip angle = 20°; slice thickness = 5 mm; four slices with a 0 mm gap; acquisition matrix = 128 x 64; 2.8 x 6.7 x 5 mm^3 voxel size; vibration frequency = 60 Hz; flow-compensated trapezoidal MEG with 27 mT/m amplitude and 16.67 ms duration (60 Hz) along the slice direction. Motion-encoding efficiency for the MEG used in this study was 16.4 μm/rad. For each slice, images were acquired with four phase offsets between MEG and vibrations with positive as well as negative encoding, resulting in eight images per slice (Figure 1). A GRAPPA acceleration factor of 2 with 24 reference lines (equivalent to R = 1.45) was utilized in MREr to reduce the breath-hold duration per slice to 8 seconds.[37] For SMS-MREr, we used MB = 2 along with an in-plane undersampling factor of 2 with eight reference lines, which were not used in the reconstruction. This resulted in a 14.4-second acquisition for four slices. A 2-second low-resolution GRE-based reference scan was acquired immediately before SMS-MREr acquisition to serve as a reference scan for split slice-GRAPPA reconstruction,[36] resulting in a total breath-hold duration of 17 seconds for the acquisition of four slices. All images were reconstructed using custom MATLAB scripts. Slice-GRAPPA and in-plane GRAPPA kernel sizes were 5 x 5 and 4 x 5, respectively. Final images were interpolated to a 256 x 256 matrix. Individual coil images were combined by using voxel-wise optimal combination based on coil sensitivities, while assuming zero noise correlation between the coils.[38] Total reconstruction time (excluding time required to load data) per dataset was 15–16 seconds on a standalone computer.

3.1.2 | Phantom experiments

To validate SMS-MREr and the phase noise measure proposed below, and to investigate different combinations of slice gap and in-plane/SMS acceleration factors, we imaged a PVC gel phantom. A cylindrical PVC gel phantom was imaged in a 1.5 T MRI scanner (Aera, Siemens). The phantom was placed in a standard head/neck coil with 24 receive channels and 60 Hz vibration was induced from the bottom of the phantom. Axial slices were acquired by encoding through-plane motion with imaging parameters identical to those used for in vivo liver MRE scans, with the exceptions noted below. MRE acquisition was performed using the following combinations of imaging sequences and parallel imaging parameters:

1. GRE-MRE with TR = 50 ms and R = 1.45 (uniform undersampling factor R_{SENSE} of 2 with 24 reference lines).
2. MREr with R = 1.45 (R_{SENSE} = 2 with 24 reference lines).
3. MREr with R = 2.28 (R_{SENSE} = 4 with 16 reference lines).
4. MREr with R = 1.88 (R_{SENSE} = 4 with 24 reference lines).
5. SMS-MREr with R = 2 and MB = 2 (separate reference scan as described above).
6. SMS-MREr with R = 1 and MB = 4 (separate reference scan as described above).

Each of the aforementioned setups was repeated with three slice gaps: 0%, 100% and 200%, resulting in 18 acquisition schemes for phantom data. Five replicates were acquired for each scheme.

3.2 | Stiffness estimation

Phase images with positive and negative MEG encoding were subtracted to obtain $PO_0, PO_{\pi/2}$, PO_π and $PO_{3\pi/2}$, where $PO_0 = \arg e^{i\left(PO_0^+ - PO_0^-\right)}$, etc. This removes phase accrual due to static field inhomogeneity as well as concomitant fields and doubles the vibration-induced phase. Stiffness

calculations were performed on an image set $\{PO_0, PO_{\pi/2}, PO_\pi, PO_{3\pi/2}\}$ using MRELab (Mayo Clinic). The displacement images were Fourier-transformed in the time domain to obtain the first harmonic displacement field. Four directional filters were applied to remove the reflected waves. (As explained in Manduca et al,[40] the directional filters are a product of radial and spatially directional components, and are oriented in time as well with Butterworth bandpass cutoff frequencies). Then a Butterworth bandpass filter with cutoff values of 2–128 waves/FOV was applied to remove the longitudinal waves. Finally, the filtered first harmonic displacement field was inverted using a 2D multimodal direct inversion (MMDI) with a 95% confidence threshold mask[41] to obtain the stiffness maps. This inversion was the same as the inline stiffness maps produced on the scanner. Identical regions of interest (ROIs) were manually drawn on SMS-MREr- and MREr-derived stiffness maps to obtain average stiffness values. The ROIs were drawn to include liver regions with adequate wave propagation, while excluding (1) major blood vessels, (2) areas affected by flow artifacts, and (3) areas with less than 95% confidence level, as determined by the MMDI algorithm. Average liver ROI size was 2289 ± 899 mm^2 per slice.
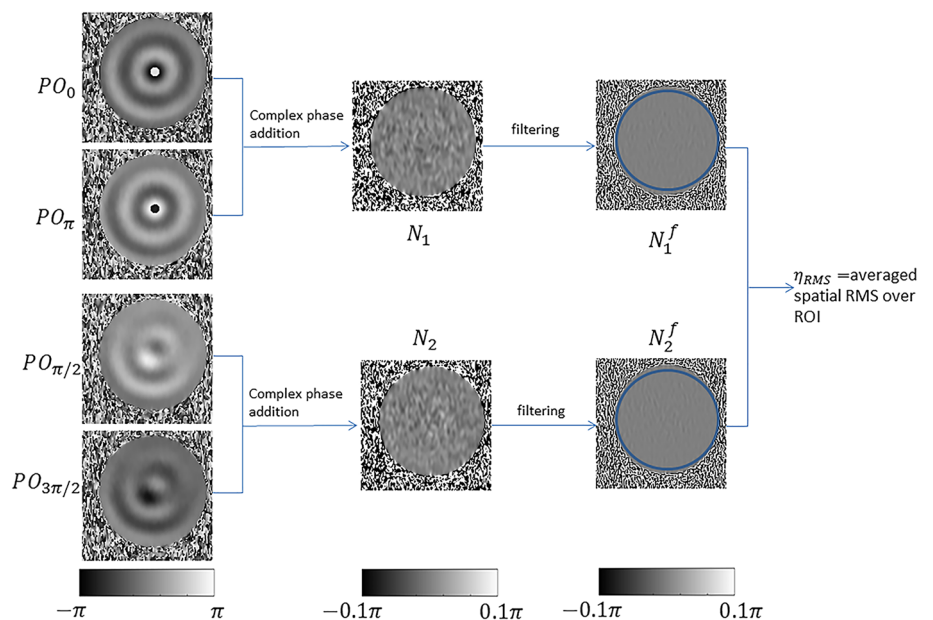
3.3 | Phase noise estimation

We developed the following approach to estimate thermal noise contribution to phase noise: images $N_1 = \arg e^{i(PO_0 + PO_\pi)}$ and $N_2 = \arg e^{i(PO_{\pi/2} + PO_{3\pi/2})}$ were obtained (Figure 3). Phase accrual due to static field inhomogeneity, concomitant field and motion sensitization due to MEGs and imaging gradients were cancelled out in $PO_0 \ldots PO_{3\pi/2}$ (Equations (1) to (3)). N_1 and N_2 therefore contain thermal noise contribution and phase accrual due to eddy currents. Additionally, imperfect alignment between images to be added can result in residual contribution of shear waves to N_1 and N_2. We therefore obtained N_1^f and N_2^f by spatially high-pass filtering N_1 and N_2 using the following kernel:

$$\frac{1}{9}\begin{bmatrix} -1 & -1 & -1 \\ -1 & 8 & -1 \\ -1 & -1 & -1 \end{bmatrix} \tag{6}$$

N_1^f and N_2^f were used as surrogates for phase noise. We define $\eta_{RMS} = \dfrac{\sqrt{\sum_{(x,y,z)\in ROI}\left(N_1^f(x,y,z)\right)^2} + \sqrt{\sum_{(x,y,z)\in ROI}\left(N_2^f(x,y,z)\right)^2}}{2 \cdot \sqrt{n_{ROI}}}$ as a heuristic measure of phase noise strength, where *ROI* represents a set of voxels within a manually drawn ROI and n_{ROI} represents the number of voxels within the ROI. Identical ROIs were drawn on MREr and SMS-MREr phase noise images to include areas without phase aliasing and flow artifacts to obtain η_{RMS} for both methods.

3.4 | G-factor estimation

We estimated g-factor and noise amplification ($g\sqrt{R}$) maps for each setup using the pseudo multiple replica-based method proposed in Robson et al[42] with some minor modifications. Briefly, the channel noise covariance matrix was computed using noise measurements, consisting of

FIGURE 3 Estimation of phase noise: estimated noise images N_2 and N_2 are obtained by adding phase difference images acquired during opposing phases of mechanical vibrations. N_1 and N_2 are filtered to remove spatially smooth variations. Averaged spatial RMS (over an ROI) of the resultant images is computed to obtain η_{RMS}

(A)

(B)
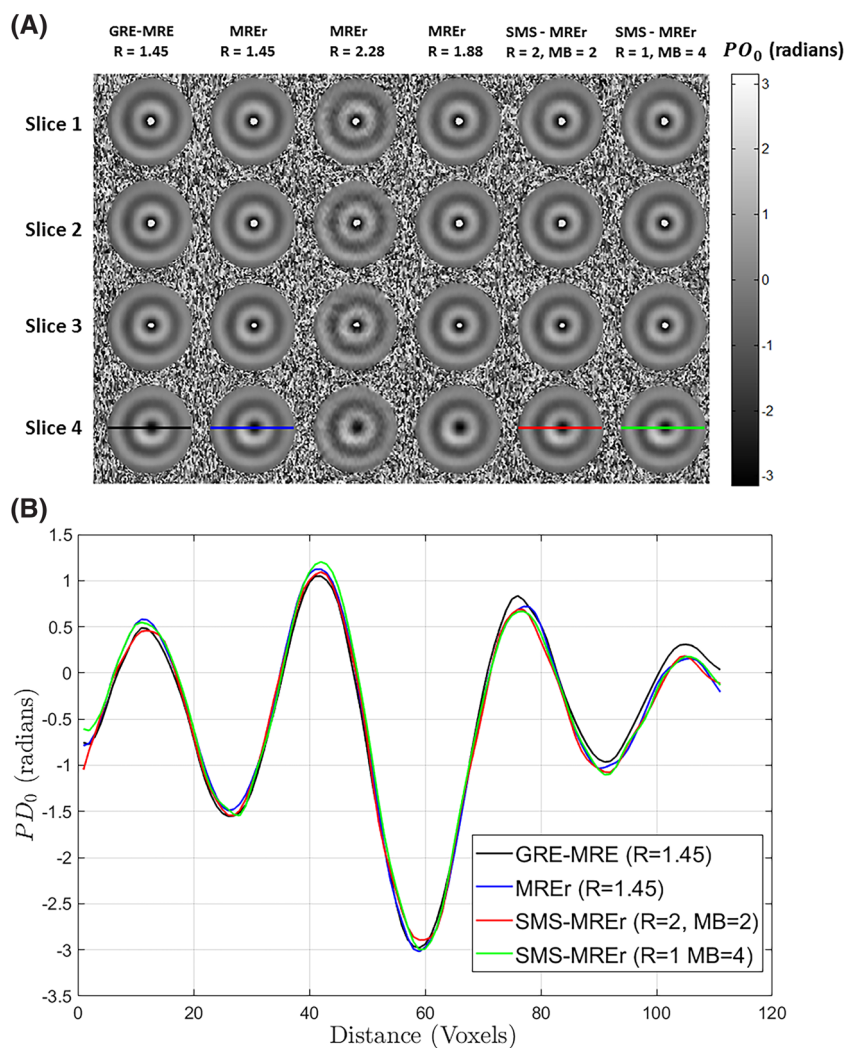
FIGURE 4 Comparison of different acquisition schemes: (A) PO_0 maps from phantom data are shown. Excellent agreement is observed between all approaches, except for rapid magnetic resonance elastography (MREr) with $R = 2.28$, which exhibits pronounced noise. Lines profiles of gradient recalled echo (GRE)-MRE as well as three MREr schemes with the greatest signal-to-noise ratio (SNR) efficiency (Table 1) are compared in (B). The results shown were obtained for a slice gap = 0. Very similar results were obtained for 100% and 200% slice gaps

(A)

(B)
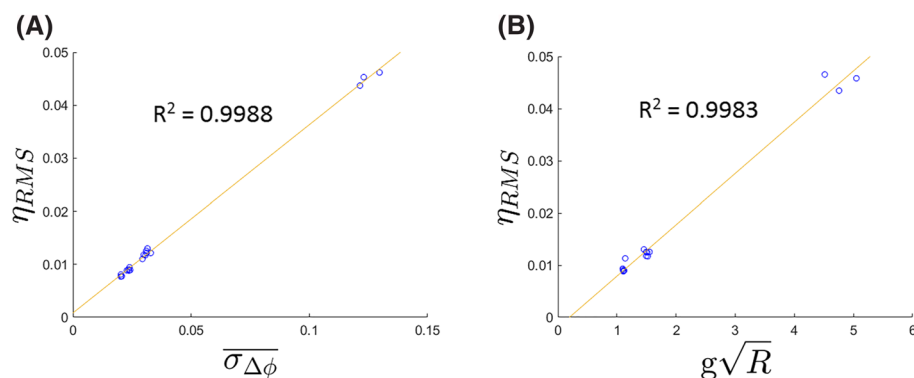
FIGURE 5 Validation of η_{RMS}. An excellent linear relationship between η_{RMS} and $g\sqrt{R}$ as well as spatially averaged phase standard deviation ($\sigma_{\Delta\phi}^-$) is observed, as seen in (A) and (B). R^2 values for η_{RMS} versus $g\sqrt{R}$ and η_{RMS} versus $\sigma_{\Delta\phi}^-$ are 0.9988 and 0.9983, respectively

256 points in the case of human data and 256 x 256 points in the case of phantom data. Pseudo replicates of complex Gaussian noise were generated by using a Cholesky factorization-based approach. We used a noise-only pseudo multiple replica instead of adding a signal component due to linearity of the entire reconstruction chain. Pseudo multiple replicas of fully sampled ($n = 250$) and accelerated data ($n = 125$) were reconstructed using the procedure identical to that used for the acquired data. GRAPPA/slice-GRAPPA weights estimated from the acquired data were used to reconstruct pseudo multiple replicas of accelerated acquisitions. Coil combination was performed as described in section 3.1. Standard deviations of real and imaginary parts of fully reconstructed pseudo random replicas were averaged to estimate the standard deviation of the noise propagated to the final reconstruction. $g\sqrt{R}$ was estimated as the ratio between the standard deviation of "accelerated" and fully sampled pseudo multiple replicas.

3.5 | Statistical analysis of liver MRE data

A paired t-test was performed to detect any systematic difference between the mean ROI stiffness values obtained using MREr and SMS-MREr. A least squares linear regression was performed to investigate the relationship between mean stiffness values obtained using both methods. Furthermore, Bland–Altman analysis was performed to investigate the agreement in mean stiffness values obtained using MREr and SMS-MREr.[43] η_{RMS} values were also compared between MREr and SMS-MREr acquisitions using a paired t-test. We also compared the percentage of reliable voxels (voxels with 95% or greater confidence level, as determined by MMDI algorithm) between MREr and SMS-MREr. First, a tissue mask was obtained for each subject, consisting of voxels with intensities above a threshold for both MREr and SMS-MREr magnitude images. Then we obtained the percentage of reliable voxels in the tissue mask for MREr and SMS-MREr, and compared those using a paired t-test.

3.6 | Validation of η_{RMS} as a measure of phase noise strength

For each acquisition scheme used for phantom data, we obtained the following:

- η_{RMS} for the first replicate.
- Spatially averaged phase standard deviation ($\bar{\sigma}_{\Delta\phi}$):
  - ○. Standard deviation maps (across five replicates) for $PO_0, PO_{\pi/2}, PO_\pi$ and $PO_{3\pi/2}$ were obtained.
  - ○. Standard deviation maps obtained in the previous step were averaged across phase offsets.
  - ○. $\bar{\sigma}_{\Delta\phi}$ was obtained by averaging the map obtained in the previous step over an ROI.

$\bar{\sigma}_{\Delta\phi}$ served as a direct measure of phase standard deviation. The linear relationship between η_{RMS} and $\bar{\sigma}_{\Delta\phi}$ was investigated to validate η_{RMS}. Furthermore, we investigated the relationship between $g\sqrt{R}$ and η_{RMS}.

3.7 | Comparison between acceleration strategies

We compared g-factor and $g\sqrt{R}$ values (averaged over an ROI) for MREr with different combinations of R and MB. We also compared relative SNR efficiency for all of the compared techniques, defined as $\frac{1}{g\sqrt{R.t_{acq}}}$, where t_{acq} represents total imaging time, including that used for reference scans.

4 | RESULTS

Table 1 shows the total acquisition time, g-factor (quartiles 1, 2 and 3), $g\sqrt{R}$ (quartiles 1, 2 and 3), SNR efficiency and average stiffness estimate for different combinations of in-plane and slice acceleration factors in a PVC gel phantom with a slice gap = 0. As expected, g-factor is lowest for R = 2 and MB = 1. Highest SNR efficiency was observed with MB = 4 and R = 1. Of all the approaches with an overall acceleration factor of >1.45, the SMS-based approaches exhibited the highest SNR efficiency. Stiffness values obtained using SMS-MREr exhibited excellent agreement with those obtained using GRE-MRE.

As can be observed from Table 1, estimated stiffness values decrease with $g\sqrt{R}$. To investigate whether this bias is caused by increased noise associated with higher acceleration factors, we estimated stiffness values from data with R = 2 and MB = 2, averaged across one, three and five repetitions, respectively (slice gap = 0), which were observed to be 5.66 ± 0.36, 5.75 ± 0.32 and 5.78 ± 0.30 kPa, respectively, for a slice, suggesting that the estimated stiffness value gets closer to that from GRE-MRE acquisition (5.77 ± 0.30 kPa) as SNR is increased through averaging.

Figure 4A shows PO_0 maps for GRE-MRE and different MREr schemes for slice gap = 0 in a PVC gel phantom. Visual comparison reveals excellent agreement between the GRE-MRE and MREr approaches, except for R = 2.28, which shows pronounced noise. Figure 4B shows line profiles from the GRE-MRE and three (SMS)-MREr schemes with the highest SNR efficiency. Excellent agreement was observed between GRE-MRE and the compared MREr schemes.

Figure 5 shows that η_{RMS} exhibits an excellent linear relationship with $\bar{\sigma}_{\Delta\phi}$ (R^2 = 0.9988) as well as $g\sqrt{R}$ (R^2 = 0.9983). This demonstrates that η_{RMS} is a valid measure of average strength of phase noise over an ROI.

Figure 6 shows magnitude and phase difference images from reconstructed MREr and SMS-MREr data. Visual inspection suggests that the simultaneously acquired images were successfully separated using the split slice-GRAPPA algorithm. Identical anatomical structures and phase patterns can be observed in MREr and SMS-MREr. However, flow artifacts are manifested in different ways in MREr and SMS-MREr images: flow

TABLE 1 Comparison between acquisition times, g, g$\sqrt{R}$, relative signal-to-noise ratio (SNR) efficiency and average PVC phantom stiffness estimates across acquisition schemes: Q1, Q2 and Q3 represent the first, second and third quartiles. Second quartile g values are used to compute SNR efficiency. Simultaneous multislice rapid magnetic resonance elastography (SMS-MREr)-based acquisitions result in the shortest scan durations, but result in higher g-factor penalties compared with MREr-based acquisitions with $R \leq 1.88$. SMS-MREr with $R = 1$ and multiband factor (MB) = 4 results in the shortest scan duration with the greatest relative SNR efficiency. Average stiffness estimates are consistent between the approaches, with the exception of MREr, with $R = 2.28$. The results shown were obtained for a slice gap = 0. Very similar results were obtained for 100% and 200% slice gaps

	MREr $R = 1.45$ (R_{SENSE} 2, 24 ref lines)	MREr $R = 2.28$ (R_{SENSE} 4, 16 ref lines)	MREr $R = 1.88$ (R_{SENSE} 4, 24 ref lines)	SMS-MREr $R = 2$, MB = 2	SMS-MREr $R = 1$, MB = 4
t_{acq} (s)	36	23	28	17	15
g	Q1 = 0.90 Q2 = 0.92 Q3 = 0.94	Q1 = 2.73 Q2 = 3.08 Q3 = 3.50	Q1 = 1.06 Q2 = 1.10 Q3 = 1.14	Q1 = 1.04 Q2 = 1.09 Q3 = 1.14	Q1 = 1.08 Q2 = 1.14 Q3 = 1.20
g$\sqrt{R}$	Q1 = 1.08 Q2 = 1.11 Q3 = 1.14	Q1 = 4.13 Q2 = 4.66 Q3 = 5.30	Q1 = 1.46 Q2 = 1.52 Q3 = 1.57	Q1 = 1.48 Q2 = 1.55 Q3 = 1.62	Q1 = 1.08 Q2 = 1.14 Q3 = 1.20
SNR efficiency = $\frac{1}{g\sqrt{R.t_{acq}}}$	0.15	0.04	0.12	0.16	0.23
Average stiffness (kPa)	5.73 ± 0.31	4.44 ± 0.81	5.67 ± 0.36	5.66 ± 0.36	5.69 ± 0.37

in MREr reconstructions results in ghosting patterns that extend into the air region, whereas the corresponding artifacts in SMS-MREr reconstructions are more localized. Line profiles from MREr and SMS-MREr phase difference images show excellent agreement (Figure 6C).

Magnitude, g-factor, wave and stiffness images from a volunteer with normal stiffness are shown in Figure 7(I). Wave and stiffness maps obtained using both methods show excellent agreement. The stiffness values obtained using MREr and SMS-MREr are 1.77 ± 0.48 and 1.84 ± 0.46 kPa, respectively. First, second and third quartile g-factor values for MREr and SMS-MREr are 1.02/1.06/1.10 and 1.32/1.43/1.52, respectively.

Figure 7(II) shows the magnitude, g-factor, wave and stiffness images from a volunteer with elevated stiffness. Again, excellent visual agreement is observed between the results obtained with both techniques. The stiffness values obtained for this volunteer using MREr and SMS-MREr are 2.84 ± 0.62 and 2.54 ± 0.59 kPa, respectively. First, second and third quartile g-factor values for MREr and SMS-MREr from the same ROI are 0.93/0.97/1.00 and 1.31/1.43/1.52, respectively

Figures 7(I) And 7(II) suggest that the results obtained using MREr and SMS-MREr are in agreement for a range of stiffness values. Indeed, an excellent linear relationship between the mean stiffness values obtained using MREr and SMS-MREr was observed, as demonstrated by a Pearson correlation coefficient of 0.93 (ie, R^2 = 0.87) (figure 8A), albeit with a slight negative bias in SMS-MREr (P = 0.02). Additionally, Bland–Altman analysis demonstrated excellent agreement between the stiffness values obtained using MREr and SMS-MREr (Figure 8B). A maximum difference of 0.39 kPa was observed between MREr- and SMS-MREr-derived mean stiffness values across all 23 subjects

η_{RMS} in in vivo data was observed to be significantly higher for SMS-MREr compared with MREr (0.0312 ± 0.0188 vs. 0.019 ± 0.0069 radians, P < 0.0001), suggesting that MREr noise levels are lower compared with SMS-MREr noise levels. First, second and third quartile g-factor values for SMS-MREr were also significantly higher than those for MREr (1.39 ± 0.22/1.53 ± 0.23/1.66 ± 0.27 vs. 0.98 ± 0.05/1.03 ± 0.06/1.09 ± 0.07, P < 0.0001). Figure S1 shows that the ratio between g-factor values of MREr and SMS-MREr has a strong linear relationship with the ratio between their η_{RMS} (R^2 = 0.77, P < 0.0001). The percentage of reliable voxels within an intensity-based tissue mask was significantly higher for MREr compared with SMS-MREr (48.4% ± 6.1% vs. 44.2% ± 5.7%, P < 0.0001).

5 | DISCUSSION

Liver MRE can benefit from accelerated acquisition. Shorter imaging times will not only result in greater patient comfort, but also help in avoiding multiple breath-hold acquisitions, which are expected to result in a loss of anatomical precision due to inconsistency between breath-holds. The proposed approach achieved these goals. In this study, we demonstrated for the first time that it was possible to combine SMS and in-plane acceleration for liver MRE. This, combined with the MREr approach, enables highly accelerated diagnostic MRE data. Higher acceleration achieved by our approach enabled single breath-hold acquisition for typical diagnostic liver MRE acquisition.
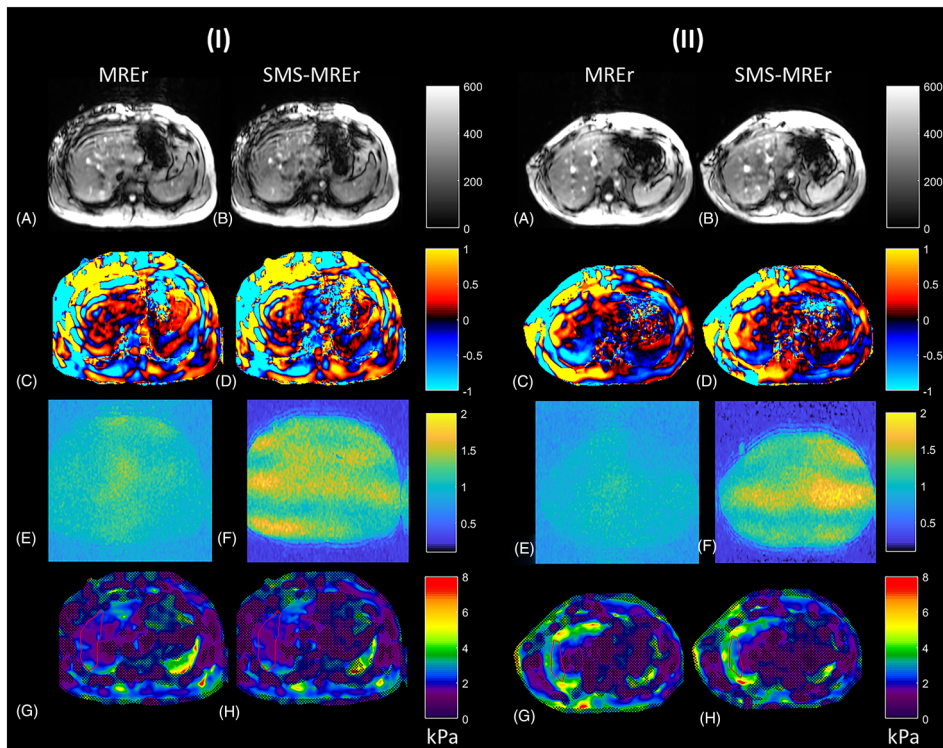
FIGURE 6 Comparison of reconstructed rapid magnetic resonance elastography (MREr) and simultaneous multislice rapid magnetic resonance elastography (SMS-MREr) images corresponding to one of the phase offsets. Slices (1, 3) and (2, 4) were acquired simultaneously for SMS-MREr. Magnitude images reconstructed from MREr and SMS-MREr show almost identical anatomical features (A). Very similar features can be seen in MREr and SMS-MREr phase difference images, particularly in the regions with high wave amplitudes (B), also evident from the line profiles (C). Phase difference images were obtained by subtracting phase images with positive and negative encoding
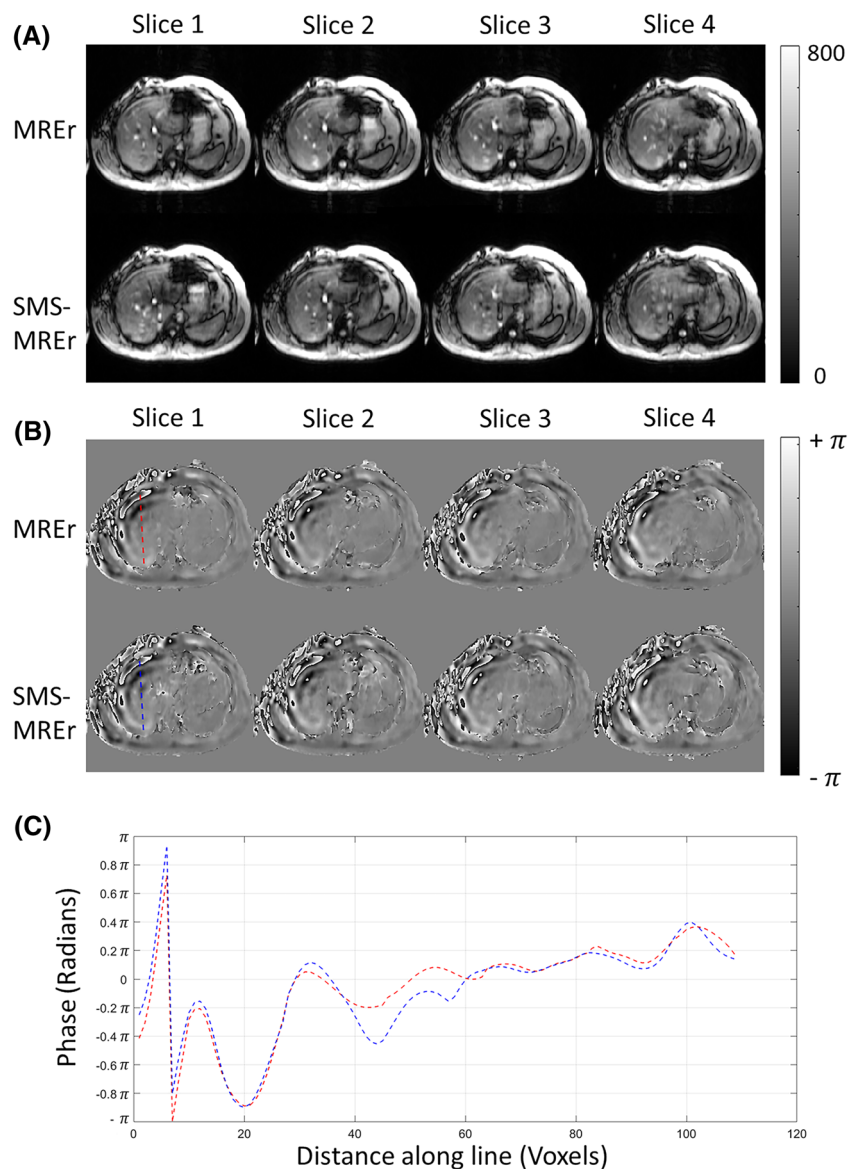

Stiffness values obtained using SMS-MREr and MREr methods exhibited high linear correlation and excellent agreement. Although SMS-MREr-derived stiffness values were lower than those obtained using MREr by 0.08 kPa, this bias is very small. This bias can be explained by the increased phase noise levels observed in SMS-MREr data, since phase variation due to noise will be interpreted by the inversion algorithm as high spatial frequency content. This explanation is consistent with the data presented in Table 1, which suggests that negative bias in stiffness estimates (compared with GRE-MRE estimates) increases monotonically with $g\sqrt{R}$. This is also supported by the fact that averaging multiple repetitions increases stiffness estimates and brings them closer to those observed with GRE-MRE. Increased noise observed in SMS-MREr can have various sources. First, SMS-MREr suffers from an additional g-factor penalty compared with MREr (Figure 5). Second, MREr acquisition includes integrated GRAPPA reference lines, which are incorporated into reconstruction. This results in an SNR gain over SMS-MREr, which relies on separately acquired reference lines.

Simultaneous excitation of closely spaced slices may result in some additional artifacts due to leakage between the spatial profiles of the bands within the pulse. However, we have found no evidence for this in vivo for the tested setting, ie, MB = 2 and R = 2. The phantom study did not reveal a contradictory result. Analysis of phantom data with four simultaneously excited slices indicates that the stiffness estimate obtained with a 0% slice gap (5.69 ± 0.37 kPa) is in excellent agreement with those obtained with 100% (5.72 ± 0.34 kPa) and 200% (5.66 ± 0.37 kPa) slice gaps. Moreover, displacement images with MB = 4 are in excellent agreement with those obtained without SMS (Figure 8). The observed consistency between MREr and SMS-MREr indicates that SMS-MREr phase difference SNR is adequate for robust stiffness estimation, despite the observed reduction in SNR.[43]

A reduced number of reliable voxels in SMS-MREr was observed compared with MREr, which also can be explained by the increased phase noise in SMS-MREr. This reduction may be of little consequence in cases where most of the voxels of interest already have a high phase contrast-

FIGURE 7 Images from subjects with normal (I) and elevated (II) stiffness. Visual inspection suggests that magnitude (A, B), wave snapshot (C, D) and stiffness (G, H) images are very similar for rapid magnetic resonance elastography (MREr) and simultaneous multislice rapid magnetic resonance elastography (SMS-MREr) for both subjects (I and II). Mean stiffness values of 1.77 ± 0.48 kPa and 1.84 ± 0.46 kPa were observed for MREr and SMS-MREr, respectively, in the subject with low stiffness (I). Stiffness values from the subject with high stiffness were 2.84 ± 0.62 kPa and 2.54 ± 0.59 kPa for MREr and SMS-MREr, respectively. These stiffness values were obtained from ROIs drawn to exclude blood vessels, areas with insufficient phase difference signal-to-noise ratio (SNR) (indicated by the checker) and areas with apparent flow artifacts. Higher g-factors are observed for SMS-MREr compared with MREr (E, F) in both cases
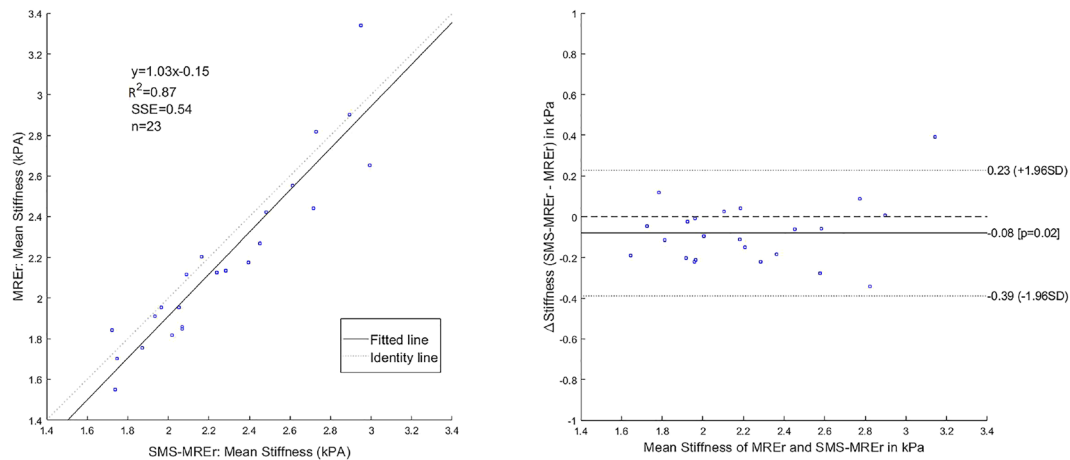
FIGURE 8 (A) Plot between rapid magnetic resonance elastography (MREr) and simultaneous multislice rapid magnetic resonance elastography (SMS-MREr) derived stiffness values. A strong linear relation is observed with $R^2 = 0.87$ with sum of squared error (SSE) = 0.54. The fitted line has slope = 1.03 and an intercept of −0.15 kPa, suggesting slight negative bias in the SMS-MREr-derived stiffness estimate. (B) Bland–Altman plot. A bias of −0.08 is observed in SMS-MREr-derived stiffness values. All bias measurements except one were found to lie within ±1.96 standard deviations from the mean bias, demonstrating excellent agreement between MREr and SMS-MREr

to-noise ratio. However, it may be necessary to use acquisitions with lower acceleration (eg, MREr only, SMS only or standard GRE-MRE) in cases where phase contrast is low due to insufficient penetration of vibrations (eg, in obese patients) or where SNR is too low (eg, in patients with a high iron load) to ensure that reliable stiffness estimates can be obtained in the regions to be evaluated.

Some of the MRE studies utilize phase-difference SNR (PDSNR) to compare SNR levels between acquisition methods.[18,44] In this approach, phase noise level is estimated based on the standard deviation of the air region. Therefore, PDSNR comparisons can be misleading when an air region is differently affected by image artifacts for the techniques to be compared, as observed in the current study. To avoid that, we have proposed the use of RMS phase noise η_{RMS} to compare phase noise levels between MREr and SMS-MREr. Calculation of η_{RMS} does not rely on any assumptions about the relationship between noise in the air region and phase noise level in tissue, and is based on direct measurement of the

RMS value of the residual phase when images with opposing phase offsets are added. Therefore, it can serve as an alternative to PDSNR in cases where the use of background noise to estimate phase noise is undesirable. There was an excellent linear relationship between η_{RMS} and $\sigma_{\overline{\Delta\phi}}$ as well as $g\sqrt{R}$, indicating that η_{RMS} is indeed a valid measure for estimating phase noise strength. One limitation of the proposed approach is that motion between the acquisition of images with different phase offsets can result in imperfect cancellation of the shear waves in N_1 and N_2. Although high-pass filtering (Figure 3) decreases spatially smooth variations in the images, residual shear-wave contribution can result in inflated η_{RMS} values. Nonetheless, this effect is randomized across acquisitions, and therefore η_{RMS} can be a valuable tool for noise comparison across techniques, even in the presence of subject motion.

Our phantom study demonstrated excellent correspondence between GRE-MRE and SMS-MREr with $R = 2$ and MB = 2 (the setting used for liver SMS-MREr acquisitions). This demonstrates the validity of SMS-MREr as an alternative to GRE-MRE, which requires 4-fold longer acquisition. Although we chose to use $R = 2$ with MB = 2 for liver data (instead of $R = 1$ and MB = 4) to avoid potential artifacts due to overlap between slice profiles of the simultaneously excited slices, our phantom study suggests that $R = 1$ with MB = 4 is the most SNR-efficient setting of all the R/MB combinations investigated in this study. This can be attributed to the fact that SMS avoids $\sqrt{R}$ penalty due to k-space undersampling.

In this study, we have focused on adding slice acceleration to further accelerate an existing MREr protocol with in-plane acceleration. However, it is possible to combine SMS (without in-plane acceleration) with other strategies for accelerated MRE. As discussed in section 2, in-plane acceleration reduces the SNR by $g\sqrt{R}$. By contrast, SMS without in-plane acceleration only results in a g-factor penalty, and therefore switching from in-plane acceleration to SMS acceleration has the advantage of increasing SNR by $\sqrt{R}$. This increased SNR can be traded for acceleration, eg, by reducing the number of phase offsets acquired or reduced motion sensitivity (fractional encoding) and shorter echo times/TR. A thorough investigation of such combinations is beyond the scope of this study.

This study has some limitations. First, the acquisition time for SMS-MREr can be further reduced: the split slice-GRAPPA algorithm does not require acquisition of integrated in-plane reference lines for simultaneously excited slices.[36] However, we did not disable the acquisition of the reference lines to allow rapid prototyping of the pulse sequence, and used the minimum number of reference lines that were allowed by the existing sequence framework. An additional reduction of 1.6 seconds could be achieved if no integrated reference lines were acquired, when using the protocol used in this study. Second, higher levels of phase noise in SMS-MREr data may become a potential problem when the signal from the liver is low due to increased iron content, or when wave penetration is limited by conditions such as obesity. Signal loss can be circumvented by using fractional encoding with a shorter TE. Attenuation of motion-related phase due to fractional encoding or reduced penetration can be overcome by using stronger actuation or systems with higher gradient amplitudes to increase motion sensitivity. Third, our cohort did not include patients, and therefore this study does not fully span the clinically relevant range of stiffness values. Fourth, although we did not find any evidence for artifacts due to interslice leakage, our study design does not allow a thorough assessment of this effect. Finally, variation between breath-holds when collecting multiple slices using MREr and all slices in a breath-hold for SMS-MREr can introduce additional differences in stiffness estimates due to: (1) change in contact area between the passive driver and the subject, and (2) spatial misalignment between the acquisitions.

Future work will focus on further improving the SMS-MREr image quality by choosing the optimal combination of in-plane and slice acceleration factors. This improved protocol will be used to assess the equivalence between MREr- and SMS-MREr-based stiffness estimates in a larger cohort, including a patient population with higher levels of liver stiffness.

In conclusion, this study has demonstrated the development of SMS along with in-plane acceleration for liver MRE application. Excellent agreement in stiffness estimates between SMS-MREr and MREr was also demonstrated, indicating that SMS-MREr can be a potential clinical tool for liver MRE to acquire four slices in a breath-hold. However, further studies with a larger cohort are still warranted.

ORCID
Waqas Majeed https://orcid.org/0000-0002-1280-0238

REFERENCES
1. Bataller R, Brenner DA. Liver fibrosis. *J Clin Invest*. 2005;115:209.
2. Fowell AJ, Iredale JP. Emerging therapies for liver fibrosis. *Dig Dis*. 2006;24:174-183.
3. Friedman SL, Bansal MB. Reversal of hepatic fibrosis—fact or fantasy? *Hepatology*. 2006;43:S82-S88.
4. Ratziu V, Charlotte F, Heurtier A, et al. Sampling variability of liver biopsy in nonalcoholic fatty liver disease. *Gastroenterology*. 2005;128:1898-1906.

5. Piccinino F, Sagnelli E, Pasquale G, et al. Complications following percutaneous liver biopsy: a multicentre retrospective study on 68 276 biopsies. *J Hepatol*. 1986;2:165-173.

6. Muthupillai R, Lomas D, Rossman P, Greenleaf JF. Magnetic resonance elastography by direct visualization of propagating acoustic strain waves. *Science*. 1995;269:1854.

7. Kolipaka A, Aggarwal SR, McGee KP, et al. Magnetic resonance elastography as a method to estimate myocardial contractility. *J Magn Reson Imaging*. 2012;36:120-127.

8. Kolipaka A, Woodrum D, Araoz PA, Ehman RL. MR elastography of the in vivo abdominal aorta: a feasibility study for comparing aortic stiffness between hypertensives and normotensives. *J Magn Reson Imaging*. 2012;35:582-586.

9. Mariappan YK, Glaser KJ, Hubmayr RD, Manduca A, Ehman RL, McGee KP. MR elastography of human lung parenchyma: technical development, theoretical modeling and in vivo validation. *J Magn Reson Imaging*. 2011;33:1351-1361.

10. McGee KP, Mariappan YK, Hubmayr RD, et al. Magnetic resonance assessment of parenchymal elasticity in normal and edematous, ventilator-injured lung. *J Appl Physiol*. 2012;113:666-676.

11. Sack I, Beierbach B, Hamhaber U, Klatt D, Braun J. Non-invasive measurement of brain viscoelasticity using magnetic resonance elastography. *NMR Biomed*. 2008;21:265-271.

12. Sinkus R, Siegmann K, Xydeas T, Tanter M, Claussen C, Fink M. MR elastography of breast lesions: understanding the solid/liquid duality can improve the specificity of contrast-enhanced MR mammography. *Magn Reson Med*. 2007;58:1135-1144.

13. Yin M, Talwalkar JA, Glaser KJ, et al. Assessment of hepatic fibrosis with magnetic resonance elastography. *Clin Gastroenterol Hepatol*. 2007;5:1207-1213.

14. Talwalkar JA. Elastography for detecting hepatic fibrosis: options and considerations. *Gastroenterology*. 2008;135:299.

15. Venkatesh SK, Yin M, Ehman RL. Magnetic resonance elastography of liver: technique, analysis, and clinical applications. *J Magn Reson Imaging*. 2013;37:544-555.

16. Yin M, Glaser KJ, Talwalkar JA, Chen J, Manduca A, Ehman RL. Hepatic MR elastography: clinical performance in a series of 1377 consecutive examinations. *Radiology*. 2015;278:114-124.

17. Loomba R, Wolfson T, Ang B, et al. Magnetic resonance elastography predicts advanced fibrosis in patients with nonalcoholic fatty liver disease: a prospective study. *Hepatology*. 2014;60:1920-1928.

18. Chamarthi SK, Raterman B, Mazumder R, et al. Rapid acquisition technique for MR elastography of the liver. *Magn Reson Imaging*. 2014;32:679-683.

19. Garteiser P, Sahebjavaher RS, Ter Beek LC, et al. Rapid acquisition of multifrequency, multislice and multidirectional MR elastography data with a fractionally encoded gradient echo sequence. *NMR Biomed*. 2013;26:1326-1335.

20. Rump J, Klatt D, Braun J, Warmuth C, Sack I. Fractional encoding of harmonic motions in MR elastography. *Magn Reson Med*. 2007;57:388-395.

21. Klatt D, Yasar TK, Royston TJ, Magin RL. Sample interval modulation for the simultaneous acquisition of displacement vector data in magnetic resonance elastography: theory and application. *Physics Med Biol*. 2013;58:8663.

22. Kearney SP, Majumdar S, Royston TJ, Klatt D. Simultaneous 3D MR elastography of the in vivo mouse brain. *Physics Med Biol*. 2017;62:7682.

23. Leitão HS, Doblas S, Garteiser P, et al. Hepatic fibrosis, inflammation, and steatosis: influence on the MR viscoelastic and diffusion parameters in patients with chronic liver disease. *Radiology*. 2016;283:98-107.

24. Fehlner A, Hirsch S, Weygandt M, et al. Increasing the spatial resolution and sensitivity of magnetic resonance elastography by correcting for subject motion and susceptibility-induced image distortions. *J Magn Reson Imaging*. 2017;46:134-141.

25. Johnson CL, McGarry MD, Van Houten EE, et al. Magnetic resonance elastography of the brain using multishot spiral readouts with self-navigated motion correction. *Magn Reson Med*. 2013;70:404-412.

26. Johnson CL, Holtrop JL, McGarry MD, et al. 3D multislab, multishot acquisition for fast, whole-brain MR elastography with high signal-to-noise efficiency. *Magn Reson Med*. 2014;71:477-485.

27. Ebersole C, Ahmad R, Rich AV, Potter LC, Dong H, Kolipaka A. A Bayesian method for accelerated magnetic resonance elastography of the liver. *Magn Reson Med*. 2018;80:1178-1188.

28. Rich A, Potter LC, Jin N, Ash J, Simonetti OP, Ahmad R. A Bayesian model for highly accelerated phase-contrast MRI. *Magn Reson Med*. 2016;76:689-701.

29. Larkman DJ, Hajnal JV, Herlihy AH, Coutts GA, Young IR, Ehnholm G. Use of multicoil arrays for separation of signal from multiple slices simultaneously excited. *J Magn Reson Imaging*. 2001;13:313-317.

30. Barth M, Breuer F, Koopmans PJ, Norris DG, Poser BA. Simultaneous multislice (SMS) imaging techniques. *Magn Reson Med*. 2016;75:63-81.

31. Feinberg DA, Setsompop K. Ultra-fast MRI of the human brain with simultaneous multi-slice imaging. *J Magn Reson*. 2013;229:90-100.

32. Guenthner C, Runge J, Sinkus R, Kozerke S. Simultaneous Multislice Acquisition for Magnetic Resonance Elastography. In: Proceedings of the 25th Annual Meeting of ISMRM, Honolulu, Hawaii, USA, 2017:1132.

33. Guenthner C, Sethi S, Troelstra M, Dokumaci AS, Sinkus R, Kozerke S. Ristretto MRE: A generalized multi-shot GRE-MRE sequence. *NMR Biomed*. 2019;32:e4049.

34. Souza SP, Szumowski J, Dumoulin CL, Plewes DP, Glover G. SIMA: simultaneous multi-slice acquisition of MR images by Hadamard-encoded excitation. *J Comput Assist Tomogr*. 1988;12:1026-1030.

35. Breuer FA, Blaimer M, Heidemann RM, Mueller MF, Griswold MA, Jakob PM. Controlled aliasing in parallel imaging results in higher acceleration (CAIPIRINHA) for multi-slice imaging. *Magn Reson Med*. 2005;53:684-691.

36. Cauley SF, Polimeni JR, Bhat H, Wald LL, Setsompop K. Interslice leakage artifact reduction technique for simultaneous multislice acquisitions. *Magn Reson Med*. 2014;72:93-102.

37. Griswold MA, Jakob PM, Heidemann RM, et al. Generalized autocalibrating partially parallel acquisitions (GRAPPA). *Magn Reson Med*. 2002;47:1202-1210.

38. Pruessmann KP, Weiger M, Scheidegger MB, Boesiger P. SENSE: sensitivity encoding for fast MRI. *Magn Reson Med*. 1999;42:952-962.

39. Brown RW, Cheng YCN, Haacke EM, Thompson MR, Venkatesan R. *Magnetic Resonance Imaging: Physical Principles and Sequence Design*. New York, NY: John Wiley & Sons; 2014.

40. Manduca A, Lake DS, Kruse SA, Ehman RL. Spatio-temporal directional filtering for improved inversion of MR elastography images. *Med Image Anal*. 2003;7:465-473.

41. Silva AM, Grimm RC, Glaser KJ, et al. Magnetic resonance elastography: evaluation of new inversion algorithm and quantitative analysis method. *Abdom Imaging*. 2015;40:810-817.

42. Robson PM, Grant AK, Madhuranthakam AJ, et al. Comprehensive quantification of signal-to-noise ratio and g-factor for image-based and k-space-based parallel imaging reconstructions. *Magn Reson Med*. 2008;60:895-907.

43. Bland JM, Altman D. Statistical methods for assessing agreement between two methods of clinical measurement. *Lancet*. 1986;327:307-310.

44. Yin M, Talwalkar JA, Glaser KJ, et al. Dynamic postprandial hepatic stiffness augmentation assessed with MR elastography in patients with chronic liver disease. *Am J Roentgenol*. 2011;197:64-70.

SUPPORTING INFORMATION

Additional supporting information may be found online in the Supporting Information section at the end of this article.